Microbreaking and airflow separation in stratified air-water pipe flow - PIV setup and initial results

Petter Vollestad[1*], Atle Jensen[1]

[1] University of Oslo, Department of Mathematics, Oslo, Norway

[*] pettervo@math.uio.no

Abstract

Simultaneous two-phase PIV of stratified air-water pipe flow is performed in order to study the effect of microscale wave breaking on the airflow above waves. This paper focuses on the experimental setup used to acquire high quality PIV results of both the gas and liquid phase, and how the PIV system is triggered to ensure that the system acquires data of the leeward side of individual wave crests, which is of interest for the analysis. Some preliminary results illustrating airflow over breaking and non-breaking waves are included. The results indicate that at moderate air flow rates, active wave breaking has a stabilizing effect on the airflow above waves, reducing the sheltered region on the leeward side of the waves and the extent of the separated airflow region compared to non-breaking waves of similar steepness.

1 Introduction

Stratified gas-liquid pipe flow is relevant for several engineering applications, especially within the oil and gas sector. Recently, simultaneous two-phase PIV has been applied to study the stratified regime in air-water pipe flow (Ayati et al., 2014; Birvalski, 2015; Vollestad et al., 2019a). This has provided spatio-temporally and phase-averaged velocity profiles, enhancing our understanding of the stratified flow regime.

Vollestad et al. (2019b) studied the phenomenon of microscale wave breaking in the stratified wavy regime of two-phase pipe flow, using PIV in the liquid phase. Microbreaking, or microscale breaking waves are small scale wave breaking events, where surface tension prevents the jet formation and air entrainment characteristic of the more energetic spilling or plunging breakers (Babanin, 2011). As microscale breaking waves do not cause air entrainment, these are difficult to detect visually. The vorticity in the crest region detected by PIV has been found to be a good way of detecting active wave breaking (Siddiqui and Loewen, 2006; Vollestad et al., 2019b).

Wave breaking transfers momentum and energy to the underlying liquid flow (both mean flow and turbulence). Wave breaking may also modify the airflow above the waves, and hence both the form drag and shear stresses which make up the interface friction (Banner, 1990; Reul et al., 2008). Hence, understanding the effect of microscale breaking on the airflow above waves is assessed to be important in accurately describing the momentum transfer between the two phases in gas-liquid pipe flow. For this reason we wish to extend the PIV system used by Vollestad et al. (2019b) to capture both the signs of small scale breaking in the liquid phase, and the simultaneous airflow in the gas phase.

In this paper details of the PIV system and some instantaneous velocity profiles obtained are presented. The aim of the PIV system is:

- Obtain high quality, simultaneous PIV data of the gas and liquid phase of two-phase pipe flow.

- Simultaneously with the PIV acquisition; obtain interface elevation measurements along a region exceeding the dominant wavelength. To correlate wave statistics with wave breaking and airflow separation.

- Trigger the PIV system so that the leeward side of the crest (of interest for the analysis) is consistently within the PIV field of view as data is acquired.

2 Experimental setup

The experiments were conducted in the hydrodynamics laboratory, at the University of Oslo. The experimental setup consists of a 31 meter long, 10 cm diameter, transparent acrylic pipe. The fluids used are air and water at atmospheric pressure. A PIV measurement section was placed 26 meters from the pipe inlet (see figure 1). In this paper we focus on the PIV measurement section and the results stemming from it. Further details on the experimental setup is provided by Ayati et al. (2014); Vollestad et al. (2019b).
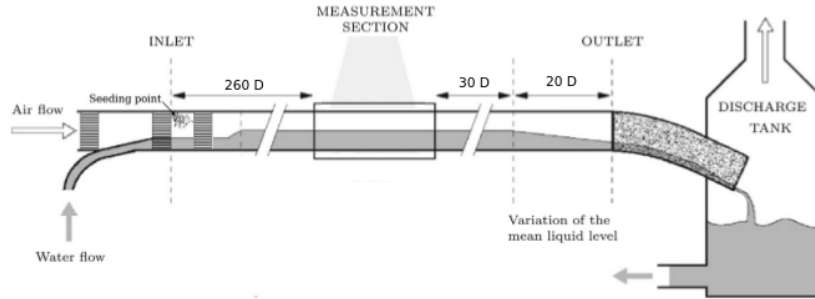

Figure 1: Overview of experimental setup.

2.1 PIV setup and processing

Simultaneous two-phase PIV (S2P-PIV) in pipes was first performed by Ayati et al. (2014), using the same flow loop and an experimental setup closely matching the setup used in the present work. While Ayati et al. (2014) demonstrated the applicability of S2P-PIV in gas-liquid pipe flow, a number of changes to the experimental setup was necessary to increase the accuracy close to the interface, and to obtain simultaneous information of the full wave profile, as well as the velocity field directly below and above the spilling region of microscale breaking waves.

A 147 mJ double pulse ND:YAG laser illuminated the centerplane of the pipe from above, while three cameras were applied to evaluate the velocity fields and the interface elevation (η) along the centerplane. The position and field of view (FOV) of the three cameras is illustrated in figure 2. The two PIV cameras are PCO.4000 cameras (4008x2672 pixels), fitted with 100 mm lenses. The liquid phase PIV camera was fitted with a 1.6x teleconverter, ensuring that the FOV of the liquid phase camera was approximately half of the gas phase camera. As a high downwards/upwards looking angle was necessary for the gas and liquid phase cameras respectively (due to the crescent shape of the waves), these were fitted with schleimpflug adapters, allowing the entire centerplane of the pipe to be in focus. A 'large-field-of-view' (LFV) camera (Nikon D7200, 6000x4000 pixels, fitted with a 28 mm lens) was applied to detect the interface over a section exceeding the dominant wavelength (λ_p) in the system (for the flow rates of interest λ_p varied from 0.2 to 0.3 m). For efficient interface detection Rhodamine B was added to the water at a concentration of $5*10^{-5}$ g/l, and the LFV camera was fitted with a filter closely matching the light emitted from the Rhodamine (B+W 041 red/orange filter). An example image from the LFV camera is presented in figure 5 a). An optical correction box half filled with water was placed around the pipe (see figure 2 c). Prior to the experiments a coordinate system was placed within the PIV section, and imaged by all cameras. The coordinate system is a combination of regular ($\Delta x = 10$ mm, $\Delta y = 15$ mm), and irregular (Δx and $\Delta y \approx$ 2-3 mm) spaced dots. The coordinate system is similar to the coordinate system used by Ayati (2015), but has been extended to account for the FOV of the LFV camera. When imaging the coordinate system by the liquid phase PIV camera the pipe was filled with water. To ensure that the coordinate system did not move as the pipe was filled with water, a circular mounting frame was designed (see figure 2 d). This included a mini lift jack that could be tightened to keep the coordinate system in a fixed location as water was introduced to the pipe.

While the two PIV cameras acquired double images (one image per laser pulse), the LFV camera was set to trigger before the first laser pulse, and had an exposure time which exceeds the Δt of the PIV acquisition, i.e. the LFV camera is double exposed. During the short Δt of the laser pulses the interface would move less than 0.1 mm, which is a negligible fraction of the overall wavelength.

As the velocity of the gas phase is approximately one order of magnitude higher than the liquid phase (excluding the spilling region of microscale breaking waves), care must be taken in setting a suitable Δt in the PIV acquisition. As seen in figure 2, the FOV of the gas-phase PIV camera is approximately twice the
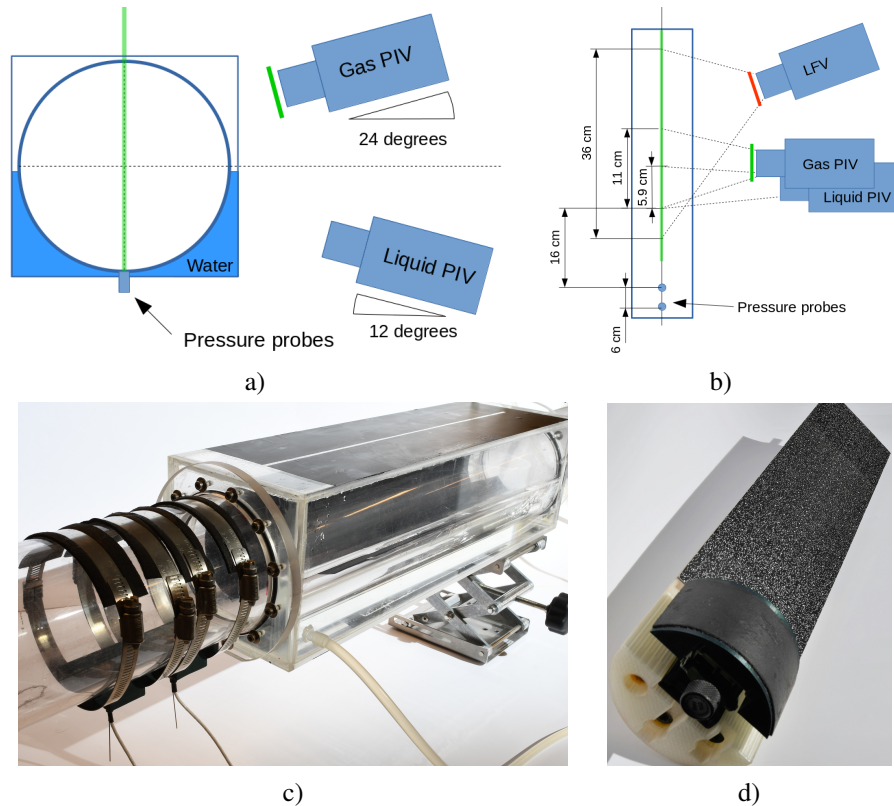
Figure 2: a-b) Overview of PIV setup. a) Seen in the streamwise direction. LFV camera located behind the gas-phase PIV camera. b) Seen from above. Green transparent line represents laser light sheet. Filters used indicated on cameras. Green: Midopt BP525 Light Green Bandpass Filter. Red: B+W 041 red/orange filter. c) Pipe section including pressure probes and optical correction box. d) Coordinate system on cylindrical mounting plate.

width of the liquid phase PIV camera, hence the maximum displacement (evaluated in pixels/Δt) of the gas-phase particles were found to be 4-5 times higher than the maximum displacement of the liquid particles. Δt was set to ensure that the gas phase particles had a maximum displacement of 18-20 px, while the liquid phase particles had a maximum displacement of 4-5 px outside the spilling region. In the spilling region of microscale breaking waves the liquid particle displacement could be up to 10 px.

Particles

The gas phase was seeded with small water droplets, generated by a high-pressure atomizer. The particles were introduced at the pipe inlet, and honeycomb flow straighteners were positioned behind the seeding point to damped out disturbances introduced by the seeder. Water is used to seed to airflow to ensure that we do not influence the surface tension of the liquid phase, and hence the characteristics of the wave formation/growth/breaking. According to the manufacturer, 72 % of the droplets are smaller than 6 μm, and the particles have been found to exhibit a stokes number well below 1 for the flow rates of interest (Ayati et al., 2014). The gas phase particles as seen in the PIV images is presented in figure 3 c).

In previous analysis of the experimental setup (Sanchis and Jensen, 2011; Ayati et al., 2014; Ayati, 2015; Vollestad et al., 2019b), 20-50 μm polyamide particles have been used as seeding particles in the liquid phase. Initial analysis using polyamide particles showed that light reflections near the interface of actively breaking waves dominated the light from the gas-phase particles near the interface. This is seen in figure 4 a). It is believed that this is caused by light scattering on the turbulent interface of an actively breaking wave. Due to the high downwards looking angle of the gas-phase PIV camera, light emitted from polyamide particles "behind" the centerplane of the pipe obstructed the gas-phase PIV images in the spilling region of the wave.

In order to avoid this issue, fluorescent particles made from a commercially available acrylic paint (Lefranc & Bourgeois, Fluorescent light orange) was used in the liquid phase, and a green bandpass fil-

ter centered at 532 nm (Midopt BP525 Light Green) was added to the gas-phase PIV camera. Particles made from the same paint was also used by Birvalski (2015). It was found necessary to remove the smallest particles from the paint/water mixture, as the high density of very small (sub μm) particles in the paint obstructed the view of the cameras, and significantly reduced the signal-to-noise ratio of the liquid phase images. The larger particles were extracted in a two-stage settling process, where approximately 20 mL of paint was added to 10 L of water. This mixture was left to settle for 12-16 hours, which allowed the larger particles to sink to the bottom. The water (including the smallest particles) was removed, and the process was repeated. After this process most of the particles were observed to be in the range of 5-20 μm diameter. An image of the particles under the microscope and as seen in the PIV images is presented in figure 3 a) and b) respectively.

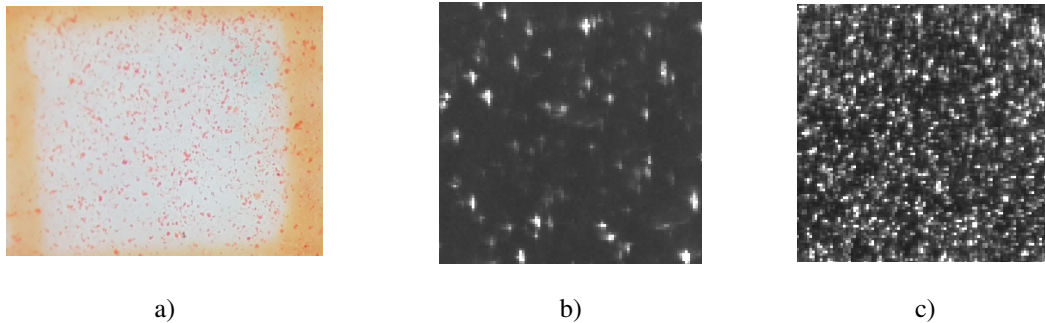a)   b)   c)

Figure 3: a) Image of liquid phase particles under the microscope, 1 mm^2 FOV. b-c) 100x100 pixels raw image of particles as seen in the experiments, for the liquid (b) and gas phase (c)

Including the fluorescent particles and green bandpass filter to the gas-phase camera significantly improved the quality of the imaging of the gas-phase near the interface, which can be seen comparing figure 4 a) and b).

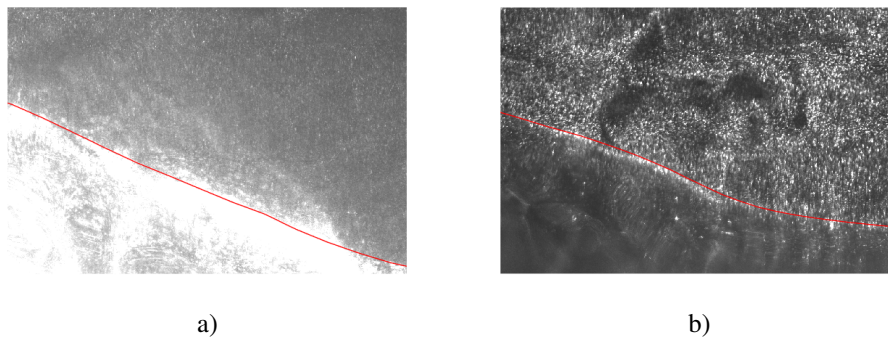a)   b)

Figure 4: Example gas-phase PIV images using polyamide particles in the liquid phase (a), and fluorescent liquid particles in combination with bandpass filter (b). Both images shows an actively breaking wave, zoomed in at the spilling region. Red line indicate detected interface.

Image processing

The gas-liquid interface was detected from the LFV camera by dividing the image into vertical sections, and scanning the image sections from top to bottom, using a combination of sobel edge-detection and a threshold value to detect the interface. An example image and interface is presented in figure 5 a). The interface was transferred to the gas and liquid PIV images using the coordinate transforms (figure 5 b-c), and the regions below/above respectively were masked out and omitted from the PIV analysis (figure 5 d-e).

As the laser light is directed from above, and hence penetrate the wavy gas-liquid interface, care must be taken in directly applying the liquid phase images for PIV. For several of the images acquired, strong light reflections were observed at the interface in the spilling region of the wave. In order to avoid that these

bright regions dominated the cross-corrolation and impacted on the PIV results, an algorithm was created for detecting and masking out coherent regions of high light intensity in the near the interface. An example of the process is presented in figure 6. Capillary ripples riding in front of the dominant wave components were found to scatter the light in the liquid phase, as seen in figure 5 b). By applying a median filter and subtracting from the original image, these variations in light intensity were reduced (see image 5 d).

a)

b)   c)

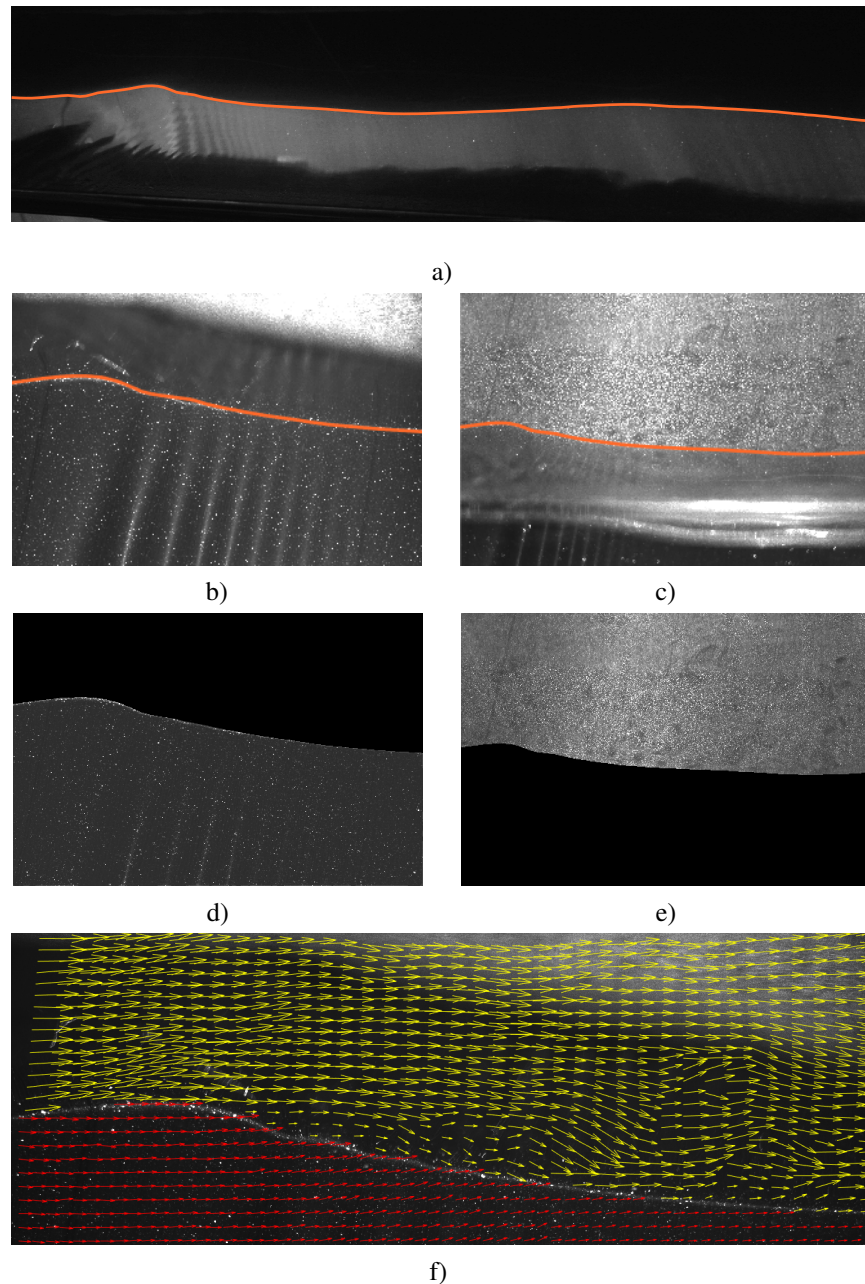d)   e)

f)

Figure 5: a-e) Example of interface detection and image pre-processing for PIV. a) Image and detected interface from the LFV camera. b-c) Raw image from the liquid (b) and gas-phase (c) camera respectively. d-e) Masked liquid (d) and gas (e) image used in cross-correlation. f) Vector field of gas (yellow arrows) and liquid (red arrows), superimposed on liquid phase PIV image. Showing 1/2 vectors in the gas phase, and 1/4 vectors in the liquid phase.

The cross-correlation was performed in Digiflow by Dalziel Research Partners, using a cascade of cross-correlation passes, with a final subwindow size of 32x32 pixels in the liquid phase, and 52x26 pixels in the
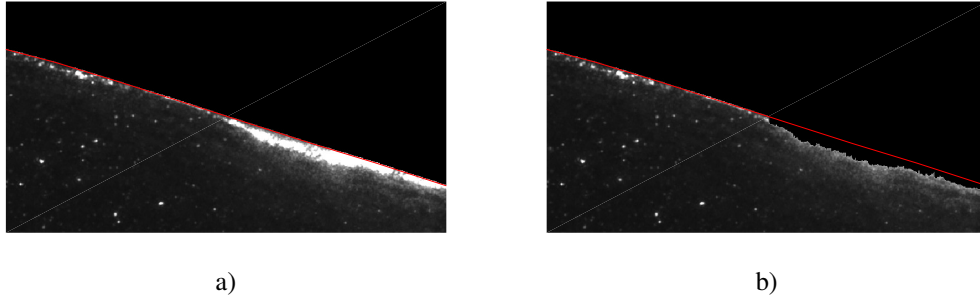
a)   b)

Figure 6: Illustration of removal of high intensity regions observed in the spilling region of microscale breaking waves. Red line: detected interface.

gas phase, using 50 % overlap. This translates to a spatial resolution of 0.24x0.24 mm^2 in the liquid phase, and 0.75x0.38 mm^2 in the gas phase. Spurious vectors were detected by local median filtering and replaced by cubic interpolation (Raffel et al., 2018).

2.2 Trigging of PIV system

Due to limitations in the data transfer rate, the PIV cameras could only acquire new double images every three seconds. We are interested in acquiring images of the leeward side of the waves, to detect signs of microscale wave breaking (Vollestad et al., 2019b). If the PIV images were acquired at a fixed rate, only a small fraction (approximately 10 %) of the images would include the full leeward side of the wave, necessary to classify the wave as either actively breaking or non-breaking according to the criterion by Vollestad et al. (2019b).

In order to limit the measurement time, and the amount of data recorded, a method to trigger the PIV system to acquire data of value to the investigation was devised. Two pressure probes (Kulite XTL-190) were mounted flush to the pipe bottom, upstream of the PIV section (position indicated in figure 2). The pressure was sampled at 2000 Hz, and normalized by a normalization filter, based on the previous 30 seconds of data. The output from the normalization filter is denoted p_n. p_n is centered at zero, and has a standard deviation of one. Neglecting pressure variations in the air-phase and dynamic pressure fluctuations, the pressure variations at the pipe bottom is directly related to the liquid height. When a pressure peak (associated with a wave crest) fulfills the criterion $\sigma < p_n$ (where σ is a threshold value, chosen as 1.4-1.6 depending on the flow rate combination), a valid wave crest is detected. At this point a cross correlation of the previous one second of data between the two pressure probes is performed, to estimate the wave propagation speed c. The wave speed is used to calculate a trigger delay, $\Delta t_{trigger} = \Delta x/c$ (where Δx is the distance to the PIV section), ensuring that the PIV system is triggered when the crest and the leeward side of the wave is within the liquid phase PIV FOV. The time development from detection of a valid crest is illustrated in figure 7.
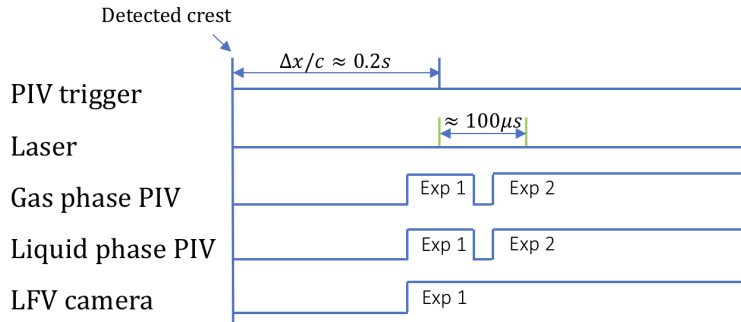

Figure 7: Schematic view of the trigging of the PIV setup, from the time a valid wave crest is detected by the trigger system.

As the propagation speed of individual waves is observed to vary in time, the triggering is not 100 % accurate. In figure 8 a) the distance from the prescribed crest position (Δx from the downstream pressure

probe), and the crest position found from the LFV interface detection for 1000 waves is presented. In table 1 the fraction of crests within $\pm$ 10, 20 and 30 mm of the target is presented. The dominant wavelength is approximately 20 cm, hence only 10 % would fall within $\pm$ 10 mm if the images were acquired at a fixed rate.

As the trigger will not activate for $\sigma < p_n$, the system introduces a bias for detecting the larger waves in the system. This bias is illustrated in figure 8 b). Here the distribution of crest heights detected by wave gauges (measuring all waves passing the measurement section) and the PIV system (measuring waves triggering the PIV system) are compared. As can be seen, the waves under analysis by the PIV system represent the larger waves in the system, and the large majority of the detected waves fulfill $\sigma\eta_{rms} < \eta_c$, where η_c and η_{rms} is the crest height (relative to the mean water level) and the rms of the interface elevation fluctuations respectively. Extracting the larger waves in the system is reasonable, as the smallest waves are very seldom found to be in a state of active breaking (Vollestad et al., 2019b), and hence will not contribute to the statistical analysis investigating the effect of breaking.

The method for assessing active wave breaking by Vollestad et al. (2019b) requires that the region $\theta = 20°$ to $80°$, where θ is the wave phase determined by a zero-crossing procedure (from $0°$ at the crest to $360°$ at the following crest), is within the liquid phase PIV FOV. The trigger method is found to ensure that this is the case for typically 70 % of all waves found to trigger the system, increasing the number of useful images acquired by a factor seven compared with acquiring at a fixed rate.
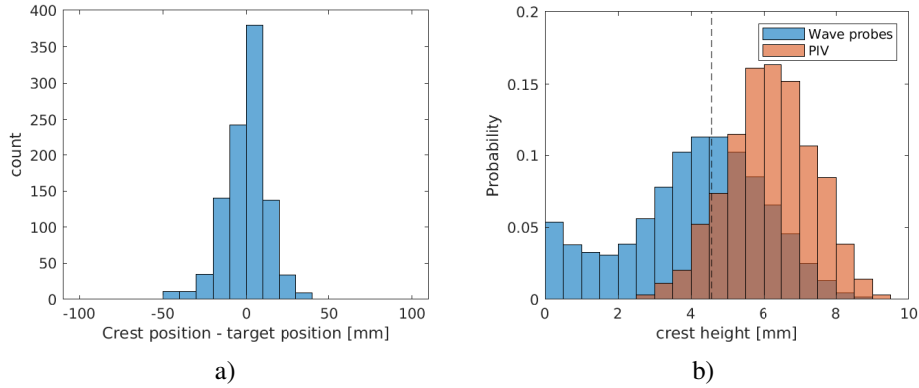

a) b)

Figure 8: Trigger statistics for $U_{sl} = 0.1$ m/s, $U_{sg} = 1.95$ m/s. a) Number of wave crests observed at 10 mm bins away from the target position. b) PDF of crest height observed by wave gauges (measuring all waves) and the PIV system (triggered at peak $p_n > 1.6$). Dashed vertical line represents $\sigma\eta_{rms}$.

Fraction of crests within +/- 10 mm from center	62.3 %
Fraction of crests within +/- 20 mm from center	90 %
Fraction of crests within +/- 30 mm from center	96.9 %

Table 1: Results from peak pressure probe triggering and peak detection

3 Example results and discussion

In this section some initial results from the analysis of one experimental case is presented and discussed. The experimental case considers gas and liquid superficial velocities (U_{sg}/U_{sl}) of 1.85 and 0.1 m/s respectively. This is slightly above the onset of microscale breaking found by Vollestad et al. (2019b). Approximately 10% of the waves passing the measurement section are in a state of active breaking. Due to space limitations a full description and analysis of the results is not included in this paper, but will be addressed in a future publication.

Figure 9 a)-b) presents instantaneous velocity fields in the gas (showing velocity vectors and vorticity contours) and liquid phase (showing vorticity contours), superimposed on the gas-phase PIV images for two waves, denoted wave A and B respectively. The full wave profile (defined from zero-up crossing to the next zero-up crossing) from the LFV camera is presented in figure 9 c).
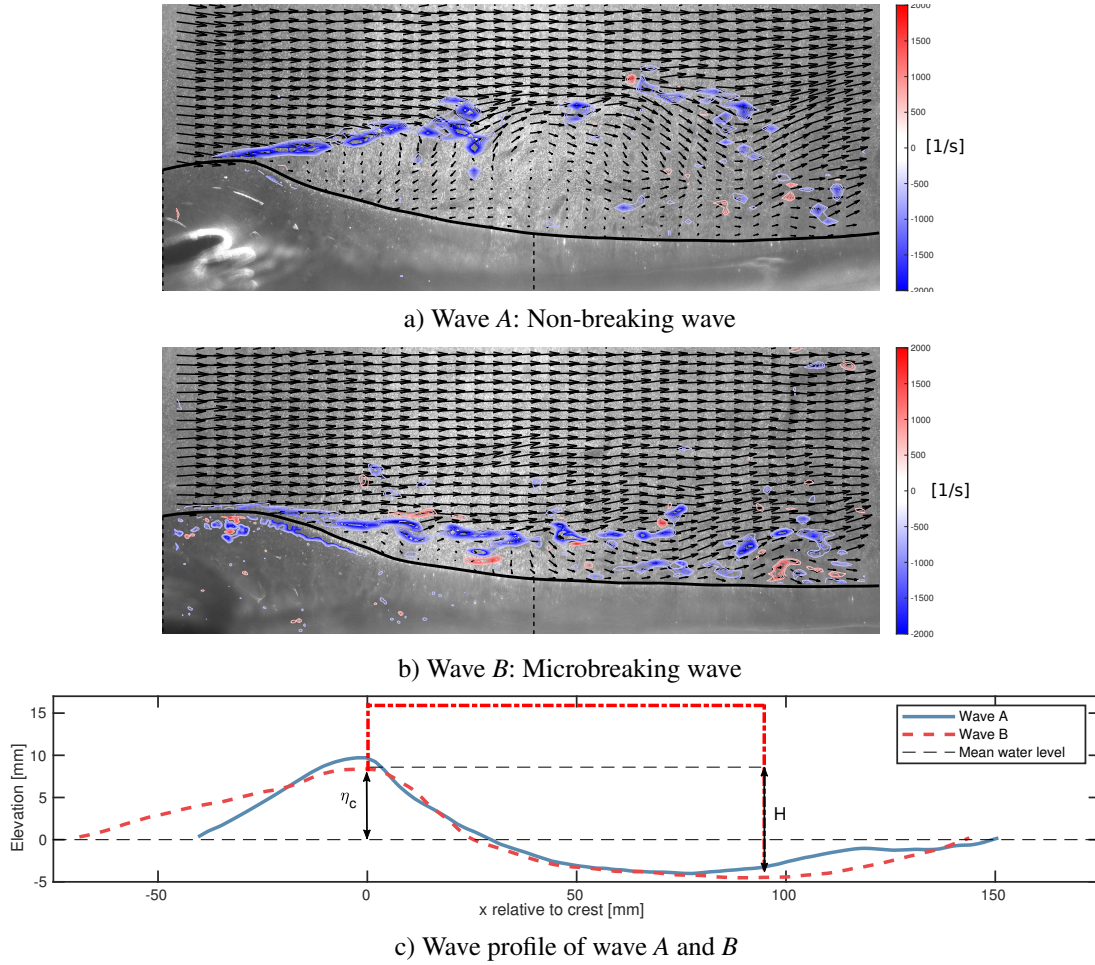
a) Wave *A*: Non-breaking wave

b) Wave *B*: Microbreaking wave

c) Wave profile of wave *A* and *B*

Figure 9: a-b) Velocity vectors in gas-phase and vorticity contours ($[\mathrm{s}^{-1}]$) in both gas and liquid phase superimposed on gas phase PIV image. Liquid vorticity multiplied by five for visibility. Showing 1/2 vectors in the gas phase. Vertical dashed lines indicate borders of liquid phase FOV. c) Wave profile from LFV camera for wave *A* and *B*. Crest height (η_c), wave height (*H*) and ROI (red dashed-dotted line) illustrated for wave *B*.

We observe that above wave *A* the airflow separates, as the shear layer is seen to leave the interface, resulting in a significant sheltered region including regions of backflow on the leeward side of the wave. For wave *B* the signs of airflow separation are much more moderate. In the liquid phase we observe that the vorticity level is fairly constant along the wave profile of wave *A*, while for wave *B*, large coherent regions of high vorticity if observed on the leeward side of the wave, and directly below the crest. This indicates that vorticity is generated by a spilling region, and swept backwards relative to the propagating wave. The wave is found to be in a state of active breaking following the criterion by Vollestad et al. (2019a). The state of breaking can also be inferred from the images of the liquid interface. For wave *A* we observe capillary ripples extending all the way to the crest, while for wave *B* the capillary ripples are displaced downstream of the spilling region, indicating that the wave is in a state of active breaking.

Table 2 summarizes some properties of the two waves. *ak* is the wave steepness, evaluated as $\pi H/\lambda$, where *H* and λ is the wave height and length respectively, and ε_{crest} is the front-face steepness, evaluated as $\Delta y/\Delta x$ from the crest to the zero-down crossing. Also listed in table 2 is the fraction of vectors within a region of interest (ROI) where the horizontal velocity is negative. The ROI is chosen from the crest to the trough in the horizontal direction, and from the interface and to a height $2*\eta_c$ (η_c is the crest height) above the mean water level in the vertical direction. The ROI for wave *B* is illustrated in figure 9 c). The results presented in figure 9 a-b) clearly show that while significant regions above the leeward side of wave *A* is propagating against the dominant flow direction, this effect is much more moderate for wave *B*. This

Wave	Microbreaking	ak	ε_{crest}	Fraction $u < 0$ in ROI
A	No	0.22	0.34	0.27
B	Yes	0.19	0.34	0.02

Table 2: Properties of the two waves presented in figure 9.

is reflected in the results in table 2, as 27% and 2% of the vectors within the ROI is observed to propagate against the dominant flow direction for wave A and B respectively.

In figure 10 a scatter plot of the fraction of the ROI with $u < 0$ versus ε_{crest} is presented for 1000 waves. Breaking and non-breaking waves (identified by the method of Vollestad et al. (2019b)) are indicated by red crosses and black circles respectively. We observe that backflow first occurs as ε_{crest} exceeds ≈ 0.1, and is moderate until $\varepsilon_{crest} > 0.2$. For high front-face steepness, backflow is occurring in a significant fraction of the ROI for both breaking and non-breaking waves, but the results indicate that the separated flow region on average is larger above non-breaking than breaking waves. Wave A and B also show this trend, but it is worth noting that they represent somewhat extreme cases of high/low sheltering for the relatively high front-face steepness of $\varepsilon_{crest} = 0.34$.
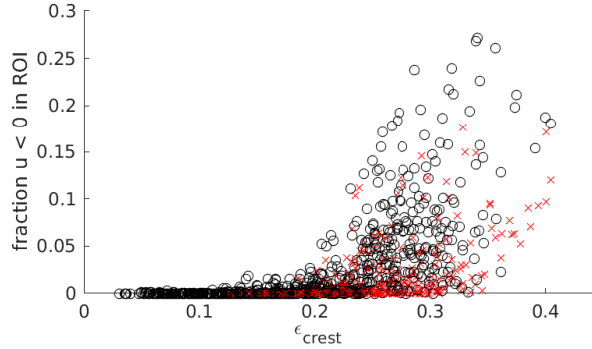

Figure 10: Scatter plot of the fraction of velocity vectors within the ROI where $u < 0$ vs ε_{crest} at $U_{sl} = 0.1$ m/s, $U_{sg} = 1.85$ m/s. o: Non-breaking wave. x: Microscale breaking waves.

Airflow separation has traditionally been linked with the onset of wave breaking (Banner, 1990), hence it is somewhat surprising to see that for a fixed front-face steepness, active wave breaking has the effect of reducing the extent of the separation bubble. There are different mechanisms that can explain this observation. As the waves break the interface geometry changes, and the actively breaking waves are observed to have a more rounded crest shape compared to the steep, non-breaking waves (this can be observed comparing figure A and B in figure 9), allowing for flow expansion without separation near the crest. As the wave breaks the liquid spills forward at a speed exceeding the wave propagation speed, and the airflow speed close to the interface. Hence, wave breaking induces a shear force on the airflow, working against the airflow separation structures.

For this moderate flow rate we observe that microscale wave breaking has the effect of modifying the airflow pattern above waves of similar geometrical properties. Airflow separation is known to enhance the form drag over waves, as it drastically increases the pressure field asymmetry relative to the wave profile (Banner, 1990), and to reduce the shear stresses in the sheltered region. To assess the overall effect of the intermittent wave breaking and airflow separation on the momentum transfer between the phases we would need measurements of the pressure field at the interface, which is outside the scope of the present study.

Acknowledgements

References

Ayati AA (2015) *Dynamics of stratified gas/liquid pipe flow*. Ph.D. thesis from the University of Oslo

Ayati AA, Kolaas J, Jensen A, and Johnson GW (2014) A PIV investigation of stratified gas-liquid flow in a horizontal pipe. *International Journal of Multiphase Flow* 61:129–143

Babanin A (2011) *Breaking and dissipation of ocean surface waves*. Cambridge University Press

Banner ML (1990) The influence of wave breaking on the surface pressure distribution in wind-wave interactions. *Journal of Fluid Mechanics* 211:463–495

Birvalski M (2015) *Experiments in stratified gas-liquid pipe flow*. Ph.D. thesis from TU Delft, Delft University of Technology

Raffel M, Willert CE, Scarano F, Kähler CJ, Wereley ST, and Kompenhans J (2018) *Particle image velocimetry: a practical guide*. Springer

Reul N, Branger H, and Giovanangeli JP (2008) Air flow structure over short-gravity breaking water waves. *Boundary-layer meteorology* 126:477–505

Sanchis A and Jensen A (2011) Dynamic masking of PIV images using the radon transform in free surface flows. *Experiments in fluids* 51:871–880

Siddiqui MHK and Loewen MR (2006) Detecting microscale breaking waves. *Measurement Science and Technology* 17:771

Vollestad P, Ayati AA, Angheluta L, LaCasce JH, and Jensen A (2019a) Experimental investigation of airflow above waves in a horizontal pipe. *International Journal of Multiphase Flow* 110:37–49

Vollestad P, Ayati AA, and Jensen A (2019b) Microscale wave breaking in stratified air-water pipe flow. *Physics of Fluids* 31:032101